RSC Advances

PAPER

View Article Online
View Journal | View Issue

Cite this: *RSC Adv.*, 2017, **7**, 27079

Oxygen-vacancy-promoted catalytic wet air oxidation of phenol from MnO_x–CeO_2†

Changjian Ma,[a] Yaoyao Wen,[a] Qingqing Yue,[a] Anqi Li,[a] Jile Fu,[a] Nouwei Zhang,*[a] Hengjun Gai,[b] Jinbao Zheng[a] and Bing H. Chen *[a]

Received 9th April 2017
Accepted 8th May 2017

DOI: 10.1039/c7ra04037g

rsc.li/rsc-advances

Catalytic oxidation can be effectively promoted by the presence of oxygen vacancies on the catalyst surface. In this study, the effect of oxygen vacancies on the catalytic wet air oxidation (CWAO) of phenol was investigated with CeO_2 and MnO_x–CeO_2 as catalysts. CeO_2 and MnO_x–CeO_2 catalysts with different amounts of oxygen vacancies were obtained *via* hydrothermal methods and applied for the CWAO of phenol. It was found that CeO_2 and MnO_x–CeO_2 nanorods were much more active than the cubic nanorods. The physicochemical properties of the samples were characterized by TEM, XRD, BET, XPS, and H_2-TPR techniques. The results revealed that the presence of oxygen vacancies in CeO_2 and MnO_x–CeO_2 catalysts could increase the oxidizing ability of the catalysts surface. The addition of Mn could greatly improve the adsorption ability of CeO_2 and more efficiently oxidize phenol and its intermediates. The synergy between Mn and Ce could further improve the catalyst redox properties and produce a larger amount of active oxygen species, which is the reason why MnO_x–CeO_2 nanorods are the most active catalysts among the catalysts investigated in this study.

1 Introduction

Phenol and its derivatives can be found as by-products from a variety of sources such as chemical, petrochemical, pharmaceutical and coal chemical industries.[1,2] Since phenol is highly toxic to aquatic life, it would result in a severe impact on water resources if phenol-contaminated streams are discharged without treatment.[3] Biotreatment is often applied in water treatment; however, phenol can inhibit the activity of microbes, causing biotreatment to be impractical for phenolic wastewater.[4] Catalytic wet air oxidation (CWAO) has been shown to be an effective and environmentally friendly way to remove refractory organic compounds, such as dyes, phenol, and succinic acid as normally no additions other than oxygen/air are needed for the process.[5–7] Under an oxygen or air atmosphere at relatively elevated temperatures and pressures, refractory organic compounds can be completely oxidized into CO_2 and H_2O or partially converted to other less toxic compounds by proper catalysts.[8,9] Clearly, developing a suitable catalyst essential for CWAO processes.

Among the various catalysts investigated for the CWAO of phenol in the reported literature, the cerium-incorporated manganese oxide composite (MnO_x–CeO_2) catalyst has been identified as one of the most promising catalysts.[10] It was reported that MnO_x–CeO_2 is an effective catalyst for the CWAO of ammonia, poly(ethylene)glycol, acetic acid, pyridine, *etc.*[11,12] Arena reported a new "redox-precipitation" route to synthesis the MnO_x–CeO_2 catalyst resulting in improved catalytic activity.[13] It was also reported that formic and acetic acids are the common intermediates during the CWAO of phenol, and that the adsorption of formic and acetic acids was driven by electrostatic interactions with the MnO_x–CeO_2 surface.[14,15] The surface reaction between the adsorbed intermediates and the activated oxygen species is the rate-determining step.[16] Furthermore, it was reported that the interaction between Mn and Ce is beneficial for the CWAO of ammonia,[11] where a physical mixture of Mn_2O_3 and CeO_2 was far less active than that of Mn/Ce catalysts. The above information shows the merits of MnO_x–CeO_2 catalysts in the field of CWAO; however, less attention has been paid to the physicochemical properties of MnO_x–CeO_2 catalysts, such as the effect of oxygen vacancies on the CWAO of phenol.

Our previous study showed that O_2 activation ability can directly affect the performance of CO oxidation.[17] The activation of oxygen can form superoxo (O^{2-}) and/or peroxo (O_2^{2-}) species, which are more oxidative than molecular oxygen (O_2). Active oxygen species can be formed on the surface of ceria in propane

[a]*Department of Chemical and Biochemical Engineering, National Engineering Laboratory for Green Chemical Productions of Alcohols-Ethers-Esters, College of Chemistry and Chemical Engineering, Xiamen University, Xiamen 361005, PR China. E-mail: zhnw@xmu.edu.cn; chenbh@xmu.edu.cn*

[b]*Qingdao University of Science and Technology, Qingdao 266042, Shandong, China*

† Electronic supplementary information (ESI) available: HRTEM images of CeO_2 110 surface, XRD patterns of MnO_x catalysts; phenol and TOC conversions on MnO_x–CeO_2 nanorods and nanocubes at various temperatures; phenol and TOC conversions on MnO_x–CeO_2 nanorods and nanocubes at various pressures. See DOI: 10.1039/c7ra04037g

oxidation passing *via* a Mars and van Krevelen mechanism.[18] Molecular oxygen prefers to fill the ceria oxygen vacancies to produce activated oxygen species.[19] High oxygen vacancy concentrations can also assist the cycle transition between Ce^{3+} and Ce^{4+} ions ($Ce^{3+} \leftrightarrow Ce^{4+}$), which is the key for many catalytic activities.

There are several ways to create oxygen vacancies. In the literature, both ceria (110) and (100) surfaces have been reported as having superior oxygen storage ability than the (111) surface.[20] However, the ceria (100) surface contains less oxygen vacancies than the (110) surface.[21] This property of the ceria (110) surface causes the improved catalytic activity for CO oxidation and soot combustion.[22,23] Doping various metals into ceria is another way to create oxygen vacancies. As Mn and Ce have a tendency to form solid solutions,[24,25] doping Mn into the ceria lattice can greatly increase oxygen mobility and also help to produce oxygen vacancies on a catalyst's surface.[26] When the atomic ratio of Mn : Ce is less than 1, all the MnO_x–CeO_2 catalysts possess the fluorite cubic structures of CeO_2.[27] Thus, doping 50% Mn atoms into CeO_2 is expected to produce the maximum amount of oxygen vacancies.

In order to study the effect of oxygen vacancies on the CWAO of phenol, we synthesized CeO_2 nanorods and nanocubes using hydrothermal methods. To further confirm the effect of oxygen vacancies on the CWAO of phenol, 50% Mn in a molar ratio was doped into CeO_2 nanorods and nanocubes to form MnO_x–CeO_2 nanorods and nanocubes. Characterizations, including XRD, H_2 temperature-programmed reduction (H_2-TPR), XPS, and TEM, were performed to link the physicochemical properties and catalytic performance. The results revealed that the oxygen-vacancy-related properties as well as the synergy between Mn and Ce are the key for the high activities in the CWAO of phenol.

2 Experimental

2.1 Preparation of the catalyst

2.1.1 Chemicals. Cerium(III) nitrate hexahydrate ($Ce(NO_3)_3 \cdot 6H_2O$), manganese(II) chloride tetrahydrate ($MnCl_2 \cdot 4H_2O$), phenol (C_6H_6O), potassium permanganate ($KMnO_4$), manganous nitrate, 50% solution ($Mn(NO_3)_2$), and acetonitrile (C_3H_3N) were purchased from Sinopharm Chemical Reagent Co. Ltd. (Shanghai, China); sodium hydroxide (NaOH) and acetic acid glacial (CH_3COOH) were purchased from Guangdong Guanghua Sci-Tech Co. Ltd. (Shantou, China). The water used in all the experiments was deionized water produced using the Millipore Milli Q system. All the reagents were used as received.

2.1.2 Material synthesis

2.1.2.1 Synthesis of CeO_2 nanorods and nanocubes. CeO_2 nanorods and nanocubes were prepared through a method similar to that reported in the literature.[28] To obtain CeO_2 nanorods, 1.736 g of $Ce(NO_3)_3 \cdot 6H_2O$ was dissolved in 10 mL of deionized water and stirred for 10 min. In a separate container, 19.2 g of NaOH was dissolved in 70 mL of deionized water, and stirred until the solution turned into a transparent color. The above two solutions were mixed and stirred for 30 min. Then, the mixed solution was transferred into a 100 mL Teflon-lined stainless autoclave and heated up to 100 °C for 24 h. After the solution was cooled to room temperature, the precipitates were separated by filtration and washed with deionized water several times. The obtained precipitates were dried at 60 °C overnight, and then calcined at 400 °C for 4 h. The procedure for the synthesis of CeO_2 nanocubes was exactly the same as for CeO_2 nanorods, except the hydrothermal condition was at 180 °C for 24 h.

2.1.2.2 Synthesis of MnO_x–CeO_2 nanorods and nanocubes. MnO_x–CeO_2 nanorods and nanocubes were synthesized through a modified method reported in the literature.[24,25] To obtain MnO_x–CeO_2 nanorods, 0.3957 g (50 mol% of Mn with respect to Ce) of $MnCl_2 \cdot 4H_2O$ and 0.868 g of $Ce(NO_3)_3 \cdot 6H_2O$ were dissolved into 5 mL and 10 mL of deionized water, respectively. Then the two solutions were mixed and stirred for 10 min. In another container, 14 g of NaOH was dissolved into 35 mL of deionized water. Then, the NaOH solution was mixed with the metal precursor solution. After stirring for 30 min, the slurry was transferred into a 100 mL Teflon-lined stainless autoclave and heated up to 120 °C for 24 h. Upon leaving the solution to cool down to room temperature, the precipitates were separated by filtration and washed by deionized water several times. The precipitates were then dried at 60 °C overnight and calcined at 400 °C for 4 h. MnO_x–CeO_2 nanocubes were synthesized using the same procedures as for the MnO_x–CeO_2 nanorods, except the hydrothermal condition was at 180 °C for 24 h.

2.1.2.3 Synthesis of MnO_2 catalysts. MnO_2 catalysts were prepared by a modified method according to the literature reported by Zhu *et al.*[29] In a typical experiment, 1.00 g of $KMnO_4$ and 0.50 g of 50 wt% $Mn(NO_3)_2$ solution were added into 64 mL of deionized water. After stirring for 10 min, the mixed solution was transferred into a 100 mL Teflon-lined stainless autoclave and kept at 160 °C for 12 h. After the solution was cooled to room temperature, the precipitates were washed and dried at 100 °C for 12 h.

2.1.2.4 Synthesis of Mn_3O_4 catalysts. Mn_3O_4 catalysts were synthesized by adding 3.22 g of 50 wt% $Mn(NO_3)_2$ solution and 1.78 g of $MnCl_2 \cdot 4H_2O$ into 10 mL of deionized water. In another container, 100 mL of 3 M NaOH solution was prepared, and then mixed with the metal precursor solution. After stirring for 1 h, the precipitates were washed using deionized water and dried at 100 °C for 12 h.

2.2 Catalyst characterization

X-ray diffraction (XRD) patterns for the cerium-based catalysts were collected on a Rigaku X-ray diffractometer and Cu Kα radiation (35 kV and 20 mA) was used as the X-ray source. The samples were scanned in the range of 10° to 80° at a scanning rate of 10° min^{-1}. X-ray photoelectron spectra (XPS) were obtained from the PHI Quantum 2000 Scanning ESCA Microprobe and the monochromatic Al Kα radiation (1846.6 eV) was used as the X-ray source. The binding energies of all the spectra were calibrated with the reference to the C 1s peak at 284.6 eV. N_2 adsorption–desorption isotherms were performed at 77 K using a Micromeritics ASAP 2020 instrument. All the samples (300

mg) were degassed at 200 °C for 2 h in vacuum before the measurements started. The specific surface areas were calculated by the Brunauer–Emmett–Teller (BET) method. Hydrogen temperature-programmed reduction (H_2-TPR) was recorded using a thermal conductivity detector (TCD). Typically, 80 mg of sample was pretreated in pure argon (Ar) at 200 °C for 2 h with a flow rate of 40 mL min^{-1}. After the temperature was cooled down to 50 °C, the gas was switched to 5% H_2/Ar with a flow rate of 40 mL min^{-1}. The temperature was then raised to 850 °C at a ramp of 10 °C min^{-1}. Transmission electron microscopy (TEM) was performed on the Tecnai F30 with an acceleration voltage of 300 kV. The specimen was prepared by dispersing the sample in ethanol solution and sonicating for 20 min. The dispersed sample was dripped on a carbon-coated copper grid and dried at room temperature. The catalyst composition was determined by inductively coupled plasma mass spectrometry (ICP-MS).

2.3 Catalytic activity measurements

The CWAO process was operated in a 100 mL temperature-programmed autoclave reactor with a magnetic-driven stirring mixer. A typical experiment was carried out as follows: 70 mL of phenol solution (1000 ppm) and 0.28 g of catalyst (4 g L^{-1}) were added into the reactor, and the reactor was purged using N_2 to remove the gaseous oxygen. The reactor was allowed to heat to the required temperature (100–180 °C) and the first sample was taken to evaluate the amount of phenol adsorbed. The desired amount of air (0.5–3.5 MPa) was then charged into the reactor, meanwhile, the time counting started. Samples were withdrawn periodically to monitor the progress of the reaction. The stirring speed was kept at 800 rotation per minute (rpm) at all times. The collected samples were filtered and the phenol concentrations were analyzed by Agilent 1100 high performance liquid chromatography (HPLC) instrument using a Dionex C_{18} column. The wavelength of the UV detector was set to 254 nm. Acetonitrile and 0.2 wt% acetic acid solution were used as the mobile phases with a total flow rate of 1 mL min^{-1}. The reaction evolutions of phenol's intermediates were also analyzed by HPLC according to the methods reported by Yang.[9] Total organic carbon (TOC) was measured by a Shimadzu TOC-L analyzer.

3 Results and discussion

3.1 Structural characterization

The TEM images of CeO_2 nanomaterials are displayed in Fig. 1. The crystal size for CeO_2 nanocubes and nanorods are 30 and 10 nm in diameter, respectively. The exposed surfaces for CeO_2 nanorods are the (110) and (100) surfaces, rather than the (100) surface for CeO_2 nanocubes. A clearer CeO_2 nanorods (110) surface image is also provided in Fig. S1.† It is obvious that CeO_2 nanorods have more "dark spots" and the surface seems "rougher" than that of the CeO_2 nanocubes. A similar phenomenon was also reported by Li, and it can be explained that the rougher surface of CeO_2 nanorods is due to the formed oxygen vacancy clusters.[19] Thus, it could be expected that CeO_2 nanorods contain more oxygen vacancies than CeO_2 nanocubes. The TEM results also indicate that the ceria (110) surface has a tendency to form more oxygen vacancies than the (100) surface, which is consistent with previous studies.[20,21]

The TEM images of MnO_x–CeO_2 nanocubes and nanorods are shown in Fig. 2. The average diameter of the MnO_x–CeO_2 nanocubes is about 17 nm, and the exposed surface is confirmed to be the (100) surface, where the inter-planar space is 0.27 nm. Fig. 2(c) and (d) are the typical images of MnO_x–CeO_2 nanorods, which have an average diameter of 10 nm. The predominant facets for the MnO_x–CeO_2 nanorods are the (111) and (100) surfaces. The surface of MnO_x–CeO_2 nanorods was also found to be "rougher" than the surface of MnO_x–CeO_2 nanocubes, which implies that MnO_x–CeO_2 nanorods have more surface reconstructions and oxygen vacancies. The existence of oxygen vacancy clusters can promote the transition from Ce^{4+} to Ce^{3+}, which generates more active oxygen species.[30] This property of CeO_2 and MnO_x–CeO_2 nanorods is expected to play an important role in the CWAO of phenol.

In order to confirm the chemical compositions of the MnO_x–CeO_2 catalysts, line-scan analysis was conducted (Fig. 3). For both MnO_x–CeO_2 nanocubes and nanorods, Mn and Ce follow the same pattern, which suggests that they may have formed solid solutions. ICP-MS analysis was performed to further verify the elemental compositions of the MnO_x–CeO_2 nanocubes and nanorods. The results show that both MnO_x–CeO_2 nanocubes and nanorods contain 48 mol% of Mn. Therefore, it was proven that MnO_x–CeO_2 nanocubes and nanorods have similar chemical compositions.

The XRD patterns of CeO_2 and the MnO_x–CeO_2 nanomaterials are presented in Fig. 4. All the catalysts have the fluorite cubic structures of CeO_2 (PDF # 34-0394), in spite of there being some minor peaks of Mn_3O_4 (PDF # 18-0803) found for the MnO_x–CeO_2 nanocubes. This indicates that less Mn has doped into the ceria lattice for MnO_x–CeO_2 nanocubes. To clarify this phenomenon, magnified (111) diffraction peaks of MnO_x–CeO_2 nanomaterials with reference to CeO_2 nanorods are illustrated in Fig. 5.

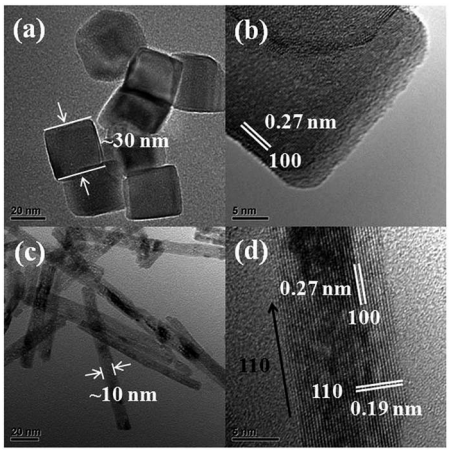

Fig. 1 TEM images of the CeO_2 nanocubes (a and b) and nanorods (c and d).

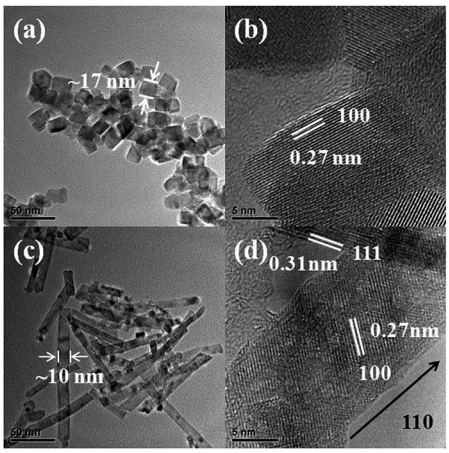

Fig. 2 TEM images of the MnO_x–CeO_2 nanocubes (a and b) and nanorods (c and d).

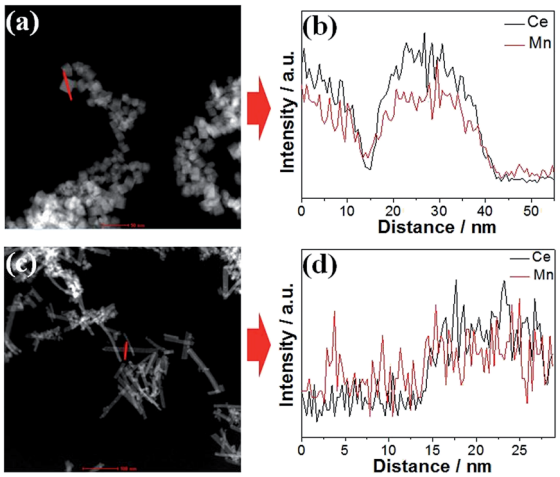

Fig. 3 Line-scan analyses of the MnO_x–CeO_2 nanocubes (a and b) and nanorods (c and d).

It was found that the diffraction peak for MnO_x–CeO_2 nanorods had shifted to a higher Bragg angle compared with MnO_x–CeO_2 nanocubes. The Bragg diffraction of each (111) peak was recorded, and each corresponding lattice parameter a was calculated (Fig. 5(b)). Indeed, the lattice parameter of the MnO_x–CeO_2 nanorods shrunk from 0.541 nm to 0.537 nm, whereas MnO_x–CeO_2 nanocubes only decreased to 0.539 nm. This further justifies that MnO_x–CeO_2 nanorods have formed a more homogeneous solid solution. Furthermore, the ionic radii of Mn ions were reported as follows: Mn^{4+}: 0.053 nm, Mn^{3+}: 0.065 nm, Mn^{2+}: 0.083 nm.[26] The ionic radii of cerium ions were: Ce^{4+}: 0.097 nm, Ce^{3+}: 0.114 nm. Thus, if more Mn is doped into Ce for the MnO_x–CeO_2 nanorods, the average ionic radius is expected to be smaller than that of MnO_x–CeO_2 nanocubes, which might cause a decrease in the lattice parameters.

Moreover, Fig. 4 also illustrates that CeO_2 and MnO_x–CeO_2 nanocubes have greater intensity than the corresponding

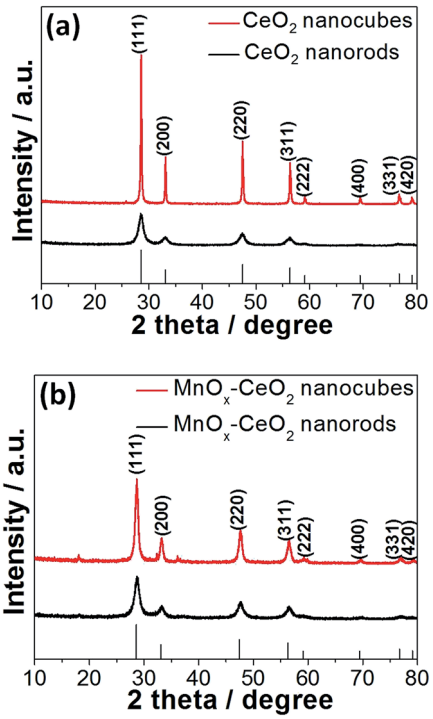

Fig. 4 XRD patterns of the CeO_2 (a) and MnO_x–CeO_2 (b) nanomaterials.

nanorods. This reveals that CeO_2 and MnO_x–CeO_2 nanorods have a higher degree of lattice defects than the corresponding cubic morphology.[8,28] This is consistent with the TEM results discussed earlier. The diffraction peaks of CeO_2 and MnO_x–CeO_2 nanorods are also relatively broader compared to the CeO_2 and MnO_x–CeO_2 nanocubes, suggesting that CeO_2 and MnO_x–CeO_2 nanorods have a smaller crystal size and would result in a higher specific surface area. This was further confirmed by the BET measurements, which show that the BET areas of CeO_2 and MnO_x–CeO_2 nanorods were 91.5 and 76.7 $m^2\ g^{-1}$, respectively. The BET areas of CeO_2 and MnO_x–CeO_2 nanocubes were 15.4 and 39.2 $m^2\ g^{-1}$, respectively. From the data shown above, it is apparent that the specific surface area was affected by the catalyst particle size. Generally, the smaller the particle size is, the larger BET surface area the catalyst possesses. As shown in Fig. 1 and 2, the particle size is increased in the following order: CeO_2 nanorods (10 nm) ≈ MnO_x–CeO_2 nanorods (10 nm) < MnO_x–CeO_2 nanocubes (17 nm) < CeO_2 nanocubes (30 nm). Therefore, the specific surface area is negatively related to the particle size: CeO_2 nanorods (91.5 $m^2\ g^{-1}$) > MnO_x–CeO_2 nanorods (76.7 $m^2\ g^{-1}$) > MnO_x–CeO_2 nanocubes (39.2 $m^2\ g^{-1}$) > CeO_2 nanocubes (15.4 $m^2\ g^{-1}$). Furthermore, as shown in Fig. 4, CeO_2 nanorods exhibited weaker XRD patterns than MnO_x–CeO_2 nanorods. This indicated that CeO_2 nanorods possessed poorer crystallinity and a smaller crystal size, although similar diameters were observed by TEM over the two catalysts. The poorer crystallinity and smaller crystal size enabled CeO_2 nanorods to have a larger BET surface area than MnO_x–CeO_2 nanorods.

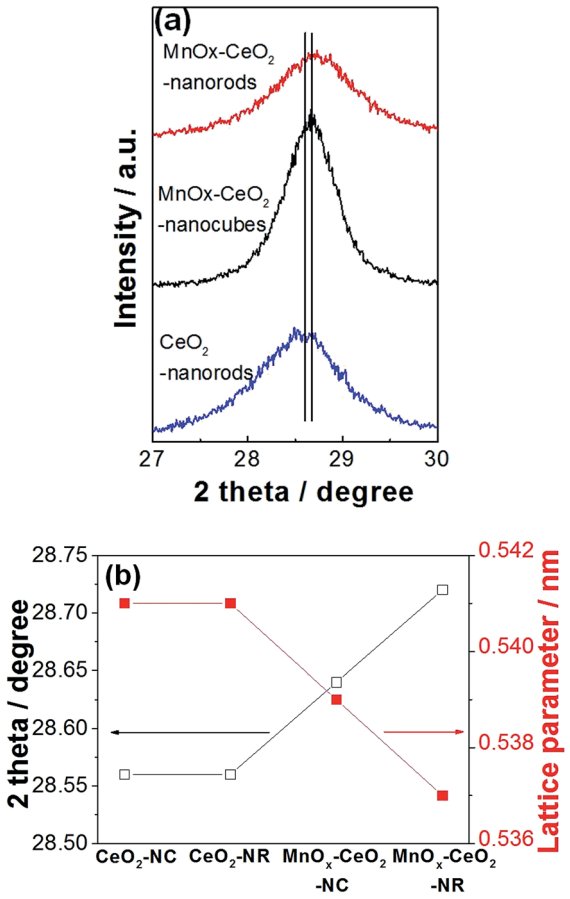

Fig. 5 Magnified (111) diffraction peaks (a) and the effect of Mn doping on cerium lattice parameters (b).

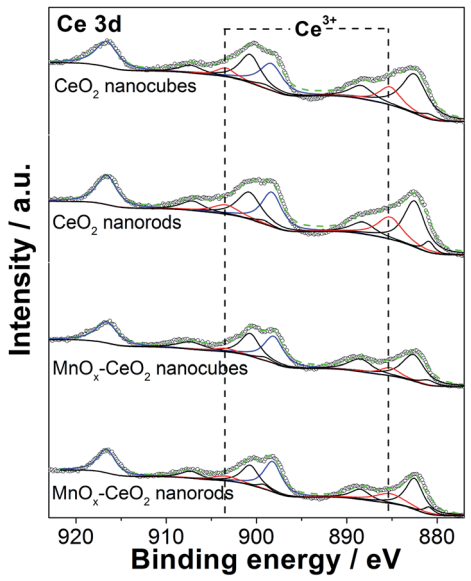

Fig. 6 Ce 3d core level XPS spectra of the CeO_2 and MnO_x–CeO_2 catalysts.

3.2 Valence state and redox properties

The XPS spectrum of Ce 3d is displayed in Fig. 6. Typically, 10 peaks were deconvoluted into pairs of spin orbit doublets. Two peaks at 916.6 and 898.2 eV are attributed to the $3d_{3/2}$, which correspond to the Ce^{4+} states. Two peaks at 903.4 and 885.2 eV are assigned to the $3d_{5/2}$, which are the Ce^{3+} states. The other six peaks at 900.7, 882.5, 907.3, 888.5, 899.2, and 880.9 eV are the satellite peaks due to the "shake down" type processes.[31] These results agree with what we found in the literature.[32] The relative portion of Ce^{3+} and Ce^{4+} valence states are summarized in Table 1. It was found that CeO_2 nanorods have 6% more Ce^{3+} ions than CeO_2 nanocubes, whereas MnO_x–CeO_2 nanorods contain 11% more Ce^{3+} ions than MnO_x–CeO_2 nanocubes. The oxygen vacancy concentration is positively related to the concentration of Ce^{3+} ions, because oxygen vacancies can reduce the thermodynamic barrier for the transition from Ce^{4+} to Ce^{3+}.[30] Thus, the XPS results are consistent with the XRD and TEM results, which helps to explain why CeO_2 and MnO_x–CeO_2 nanorods have rougher surfaces.

The Mn 2p spectra of the MnO_x–CeO_2 catalysts are shown in Fig. 7. The three peaks of Mn $2p_{3/2}$ are located at 640.8, 641.8, and 643.9 eV, corresponding to Mn^{2+}, Mn^{3+}, and Mn^{4+}, respectively.[33–35] The Mn $2p_{1/2}$ peak is centered at 653.3 eV, with a splitting energy of 11.45, based on the Mn $2p_{3/2}$. By estimating the area of each Mn species, Table 1 shows that MnO_x–CeO_2 nanorods contain a larger portion of higher valence Mn species, whereas the corresponding Mn^{4+}, Mn^{3+}, and Mn^{2+} ion abundances are 23%, 62%, and 15%, respectively. Conversely, MnO_x–CeO_2 nanocubes prefer lower valence Mn species, and the corresponding portions of Mn^{4+}, Mn^{3+}, and Mn^{2+} are 14%, 36%, and 50%, respectively.

It was also found that the Ce^{3+} concentration was suppressed when Mn was added. This effect was also reported by Larachi, where the addition of Mn caused an increase in surface Ce^{4+} concentration.[36] This phenomenon can be explained by the fact that electrons are transferred from Ce to Mn, which can decrease the concentration of Ce^{3+} and increase the concentration of Mn^{2+} or Mn^{3+}. Compared to MnO_x–CeO_2 nanorods, the Ce^{3+} concentration of MnO_x–CeO_2 nanocubes was suppressed to a higher extent, and a much greater fraction of Mn^{2+} was observed. This also suggests that more electrons are transferred from Ce to Mn for MnO_x–CeO_2 nanocubes.

Noted that the Mn^{3+}/Mn^{2+} that are incorporated into the CeO_2 lattice sites also contribute to the oxygen vacancies formation. MnO_x–CeO_2 nanocubes contained more Mn^{2+} species, but showed lower oxygen vacancies concentration than MnO_x–CeO_2 nanorods. Two possible reasons were responsible for the lower concentration of oxygen vacancies over MnO_x–CeO_2 nanocubes. First, some part of the Mn was not incorporated into the CeO_2 lattice for the MnO_x–CeO_2 nanocubes. Mn_3O_4 was detected by XRD, as shown in Fig. 4(b). It is well known that Mn_3O_4 is composed of both Mn^{3+} and Mn^{2+}.[37,38] Some Mn^{3+}/Mn^{2+} species come from the phase-segregated Mn_3O_4. These lower valence Mn species must not contribute to the formation of oxygen vacancies, since they were not in the CeO_2 lattice. Second, when Mn is doped into CeO_2, electrons

Table 1 Relative abundance of the different species obtained from the XPS data for each catalyst

Catalyst label	Ce^{3+} (%)	Mn^{4+} (%)	Mn^{3+} (%)	Mn^{2+} (%)	O_{active} (%)
CeO_2 nanocubes	32	—	—	—	16
CeO_2 nanorods	38	—	—	—	20
$MnCeO_x$ nanocubes	19	14	36	50	18
$MnCeO_x$ nanorods	30	23	62	15	26

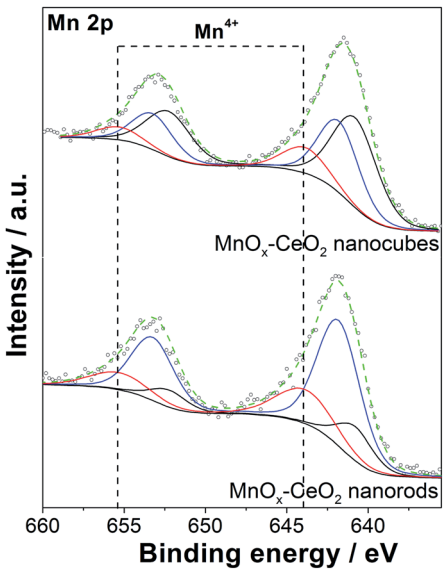

Fig. 7 Mn 2p core level XPS spectra of the MnO_x–CeO_2 catalysts.

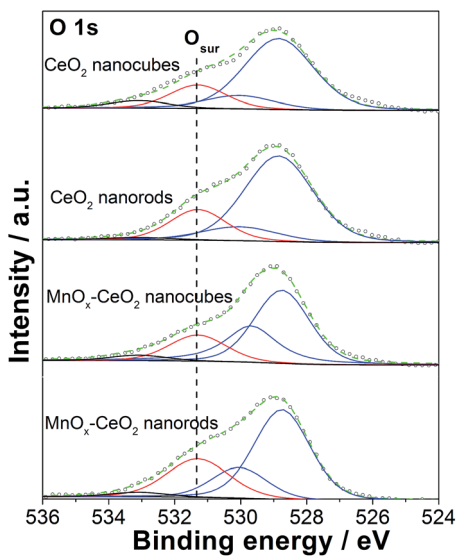

Fig. 8 O 1s core level XPS spectra of the CeO_2 and MnO_x–CeO_2 catalysts.

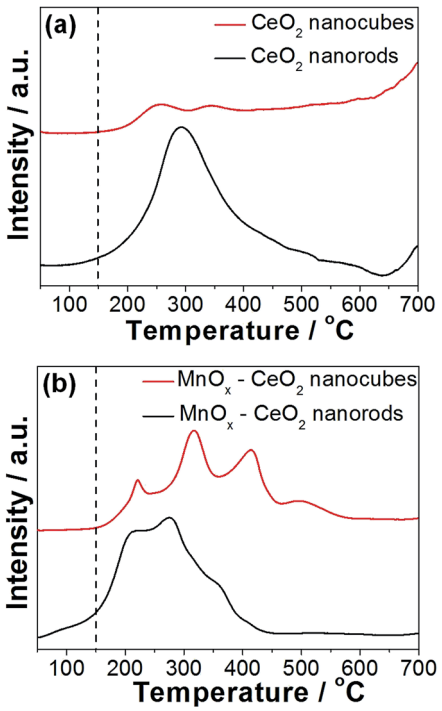

Fig. 9 H_2-TPR results of the CeO_2 (a) and MnO_x–CeO_2 (b) catalysts.

Table 2 Summary of the catalytic activity of different metal oxides on the CWAO of phenol. Phenol concentration: 1000 ppm; catalyst loading: 4 g L^{-1}; temperature: 140 °C; pressure: 2 MPa air; time: 1 h

Catalyst label	Phenol conversion (%)	TOC conversion (%)
CeO_2 nanocubes	8	6
CeO_2 nanorods	27	23
MnO_2	79	67
Mn_3O_4	70	62
$MnCeO_x$ nanocubes	100	97
$MnCeO_x$ nanorods	100	98

were transferred from Ce to Mn and the Ce^{3+} fraction was decreased from 32% to 19%. Some oxygen vacancies over Mn^{3+}/Mn^{2+} were produced at the expense of those over Ce^{3+} sites. Therefore, although a higher concentration of low valence Mn species was detected by XPS, the MnO_x–CeO_2 nanocubes still exhibited a lower concentration of oxygen vacancies. In the case of MnO_x–CeO_2 nanorods, electron transfer between Mn and Ce was also observed. However, the electron transfer was less significant than that over MnO_x–CeO_2 nanocubes. After the addition of Mn, the Ce^{3+} fraction was still up to 30%. Additionally, most of Mn was incorporated into the CeO_2 lattice for the MnO_x–CeO_2 nanorods, as proved by the XRD results. Thus,

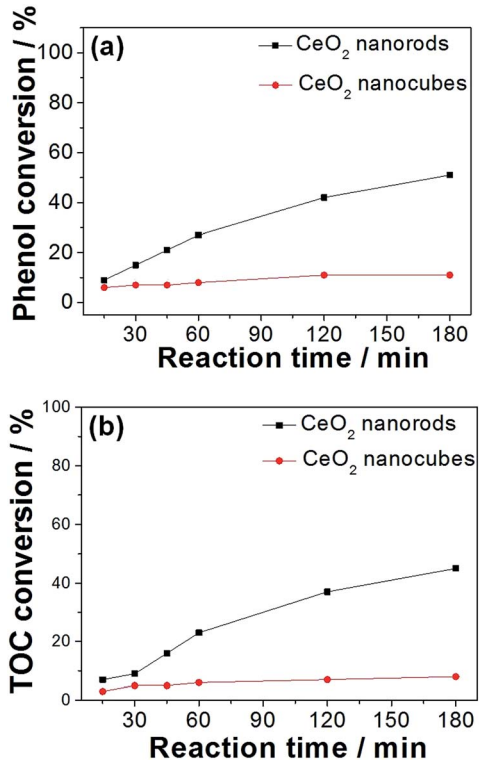

Fig. 10 The CWAO of phenol using CeO_2 nanorods and nanocubes, (a) phenol conversion, (b) TOC conversion. Concentration of phenol: 1000 ppm; catalyst loading: 4 g L^{-1}; temperature: 140 °C; pressure: 2 MPa air.

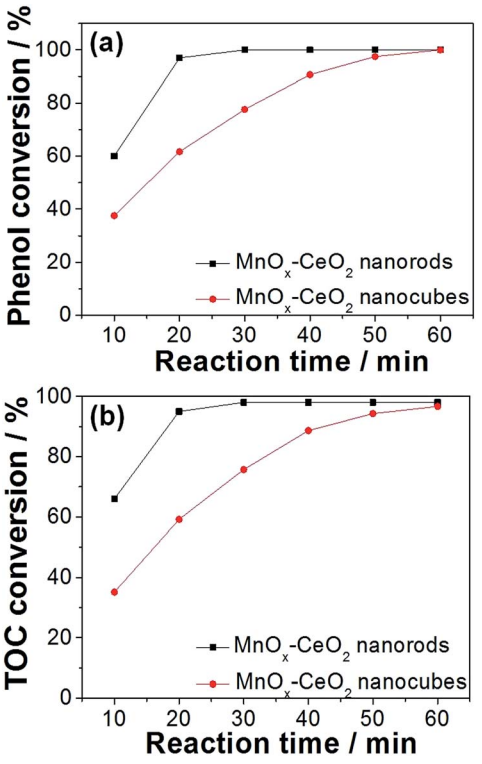

Fig. 11 Phenol (a) and TOC (b) conversions on MnO_x–CeO_2 nanorods and nanocubes. Concentration of phenol: 1000 ppm; catalyst loading: 4 g L^{-1}; temperature: 140 °C; pressure: 2 MPa air.

Mn^{3+}/Mn^{2+} might have contributed to the formation of oxygen vacancies for the MnO_x–CeO_2 nanorods.

Fig. 8 shows the O 1s spectra for the CeO_2 and MnO_x–CeO_2 nanomaterials. The peaks appearing at 528.9 and 530 eV are the lattice oxygen of the CeO_2 and MnO_x–CeO_2 catalysts.[39] The peak at 531.4 eV is the adsorbed active oxygen species, the peroxo species (O_2^{2-}), and the superoxo species (O_2^-).[40] The remaining peak at 533 eV is attributed to the adsorbed surface hydroxyl and water species. For the CeO_2 catalysts, CeO_2 nanorods possess 20% surface active oxygen, where CeO_2 nanocubes have 16%. It is reported that oxygen vacancies can promote the formation of Ce^{3+}, and that Ce^{3+} can induce the formation of active oxygen species.[41] Thus, the cause of the higher active oxygen percentage for CeO_2 nanorods might be due to the oxygen vacancies formed on the CeO_2 nanorods surface. A similar trend was also observed for the MnO_x–CeO_2 catalysts, where MnO_x–CeO_2 nanorods contained 8% more active surface oxygen than MnO_x–CeO_2 nanocubes. It is also reported that active oxygen species can be created at the interface between the CeO_2 lattice and MnO_x.[26] It is reasonable that more active oxygen species are found in MnO_x–CeO_2 nanorods, due to the synergy of Mn/Ce (more –MnO–Ce– bonds) and the higher Ce^{3+} concentration.

The redox properties of the CeO_2 and MnO_x–CeO_2 catalysts were studied by H_2-TPR experiments, and the results are displayed in Fig. 9. It is widely accepted that the low temperature reduction peak of CeO_2 nanomaterials relates to the removal of surface capping oxygens, while the high temperature reduction peak is related to the bulk oxygen.[42,43] It was observed that CeO_2 nanorods are able to remove surface oxygen at 100 °C, while CeO_2 nanocubes start to reduce at 150 °C. This indicates that CeO_2 nanorods have more reducible surface Ce^{4+} ions compared with that of CeO_2 nanocubes, which is attributed to the oxygen vacancies formed on the CeO_2 nanorods surface, because oxygen vacancies can boost the transition from Ce^{4+} to Ce^{3+}.

Doping Mn into the Ce lattice can improve the reducibility of the catalyst surface,[27] which can clearly be observed in Fig. 9(b). The reduction peak of MnO_x–CeO_2 nanorods starts at 50 °C, while MnO_x–CeO_2 nanocubes start to reduce at 150 °C. Four reduction peaks were obtained for each MnO_x–CeO_2 catalyst. For MnO_x–CeO_2 nanorods, the peak at 200 °C is attributed to the reduction of MnO_2 to Mn_2O_3. The second peak at 272 °C is assigned to the reduction of Mn_2O_3 to Mn_3O_4. The third peak at 360 °C is the mixed reduction of Mn_3O_4 to MnO and surface Ce^{4+} to Ce^{3+}, while the high temperature reduction peak at 410 °C is the reduction of the bulk Ce^{4+} to Ce^{3+}.[35,44]

The reduction peaks for MnO_x–CeO_2 nanocubes followed a similar pattern as that of the MnO_x–CeO_2 nanorods. It was found that MnO_2 was first reduced to Mn_2O_3 at 220 °C, and then Mn_2O_3 was reduced to Mn_3O_4 at 315 °C. The third peak at 415 °C is due to the reduction of Mn_3O_4 to MnO. The reduction of surface Ce^{4+} was shifted to a high temperature around 500 °C

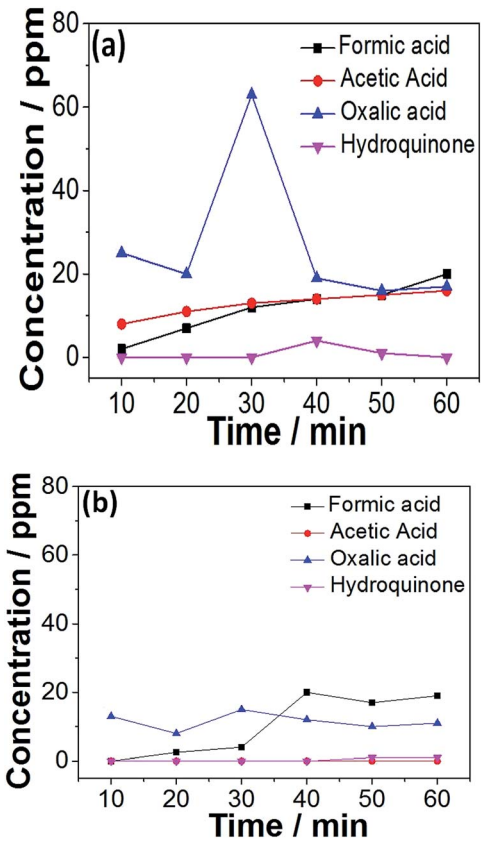

Fig. 12 Evolution of the small-molecule intermediates in the CWAO of phenol over MnO_x–CeO_2 nanorods (a) and nanocubes (b).

due to the lower concentration of Ce^{3+} and the electron transfer from Ce to Mn. Compared to the reduction peaks of MnO_x–CeO_2 nanorods, all of the reduction peaks for MnO_x–CeO_2 nanocubes have shifted to higher temperatures. This is reasonable since more Mn has entered the Ce lattice for MnO_x–CeO_2 nanorods, which causes the formation of –Mn–O–Ce– bonds. It was reported that –Mn–O–Ce– bonds is more reducible than –Ce–O– or –Mn–O– bonds.[26] The presence of –Mn–O–Ce– bonds effectively lowered the overall reduction temperature for MnO_x–CeO_2 nanorods.

It is interesting that MnO_x–CeO_2 nanorods also possess more compacted reduction peaks than MnO_x–CeO_2 nanocubes. This might be due to the greater abundance of Mn^{4+} and Mn^{3+} of MnO_x–CeO_2 nanorods, because higher oxidation states of Mn are easier to be reduced. Another possible explanation is that oxygen vacancies in MnO_x–CeO_2 nanorods could also promote the transition of Mn from 4 + to lower valence states, since it is able to lower the thermodynamic barrier for $Ce^{4+} \rightarrow Ce^{3+}$.

3.3 Catalytic wet air oxidation of phenol

The catalytic performance of various oxides were investigated and the results are displayed in Table 2. It was found that cerium and manganese monoxides (Fig. S2†) exhibit much lower activities for the CWAO of phenol than the MnO_x–CeO_2 catalysts, which proves the effectiveness of Mn/Ce oxide composites. In order to study the effect of oxygen vacancies on the CWAO of phenol, CeO_2 nanorods and nanocubes were carefully investigated. The adsorption experiments showed that CeO_2 nanorods could absorb 5% of phenol, whereas CeO_2 nanocubes could only absorb 1%. Fig. 10 illustrates the reaction profiles of phenol and TOC conversions for CeO_2 nanomaterials at 140 °C and 2 MPa air. It was found that CeO_2 nanocubes were almost inert toward the CWAO of phenol, whereas phenol and total organic carbon (TOC) conversions were 11% and 8%, respectively. Conversely, CeO_2 nanorods were more active than CeO_2 nanocubes, whereas 51% of phenol conversion and 45% of TOC removal were achieved.

Compared to CeO_2 nanomaterials, MnO_x–CeO_2 catalysts give very rapid phenol oxidation. MnO_x–CeO_2 nanorods could completely convert phenol and remove 98% of TOC within 30 min, at 140 °C and 2 MPa air (Fig. 11). The comparable activity for MnO_x–CeO_2 nanocubes could only be achieved after 60 min. Furthermore, the adsorption experiment showed that MnO_x–CeO_2 nanorods could absorb 15% of phenol, whereas MnO_x–CeO_2 nanocubes only absorbed 7%. It was seen that the addition of Mn could enhance the adsorption ability of CeO_2 nanorods by more than 3 times. This is important, since adsorption is the primary step for the CWAO of phenol. Moreover, it was reported that high oxidation states of manganese oxide can also behave as active centers for phenol oxidation.[36] Thus, it could be postulated that the addition of Mn helped to adsorb phenol and its intermediates, then Mn^{4+} was reduced and the adsorbed organic compounds were oxidized.

Tests on the evolution of the small-molecule intermediates for MnO_x–CeO_2 catalysts were conducted, and the results are shown in Fig. 12. There are 4 major small-molecule intermediates: formic acid, acetic acid, oxalic acid, and hydroquinone. Other intermediates, including polymeric products, are also reported in the literature,[45] and can be calculated by subtracting the concentration of the remaining TOC and small-molecule intermediates. The initial TOC value for phenolic solution was about 850 ppm. For MnO_x–CeO_2 nanorods, the TOC conversion was 98%, and the remaining TOC was calculated to be 17 ppm. The total organic carbon concentration of formic acid, acetic acid, oxalic acid, and hydroquinone was also converted, and turned out to be 15 ppm. Thus, it implies that the small-molecule intermediates are responsible for 88% of the remaining TOC for MnO_x–CeO_2 nanorods. On the other hand, the small-molecule intermediates are only responsible for 32% of the remaining TOC for MnO_x–CeO_2 nanocubes. This means MnO_x–CeO_2 nanocubes have converted more phenol into large-molecule intermediates. In other words, MnO_x–CeO_2 nanocubes are less oxidative than MnO_x–CeO_2 nanorods.

The MnO_x–CeO_2 catalysts were also examined by comparing their catalytic activities at various temperatures (Fig. S3†). The results show that the catalytic activity of MnO_x–CeO_2 nanorods and nanocubes are both positively related to the reaction temperature. MnO_x–CeO_2 nanorods and nanocubes exhibit similar catalytic activity at 100 and 180 °C. However, MnO_x–CeO_2 nanorods become much more active than MnO_x–CeO_2 nanocubes at 140 °C. This can be due to the high reducibility of

MnO_x–CeO_2 nanorods surface, which play a more important role at moderate temperature.

In order to study the effect of oxygen partial pressure in the CWAO of phenol on MnO_x–CeO_2 nanorods and nanocubes, different pressures were investigated (Fig. S4†) for reaction. The temperature was kept at 140 °C and the catalytic activity was measured after 30 min reaction. When the total air pressure was set to 0.5 MPa, MnO_x–CeO_2 nanorods could convert 83% of phenol and 71% of TOC, whereas MnO_x–CeO_2 nanocubes could only convert 64% of phenol and 62% of TOC. When the pressure was increased, both the MnO_x–CeO_2 nanorods and nanocubes exhibited higher phenol and TOC conversions. MnO_x–CeO_2 nanorods could completely remove phenol when the total pressure was greater than 2 MPa air. On the other hand, MnO_x–CeO_2 nanocubes could only achieve 95.7% phenol conversion at 3.5 MPa air. These phenomena emphasize the importance of the oxygen partial pressure to the performance of MnO_x–CeO_2 catalyst materials.

For the CWAO of phenol, the oxidizing ability of the catalyst plays a decisive role in the whole CWAO process. The TEM and XPS results indicated that the two nanorods catalysts presented a higher amount of oxygen vacancies, while the H2-TPR results suggested that both nanorod catalysts possessed higher reducibility. Generally, the lower temperature at which the reduction peak appears, the higher the oxidizing ability the catalyst possesses. Clearly, increasing the oxygen vacancies concentration can promote the oxidizing ability and thus enhance the catalytic performance for the CWAO of phenol.

4 Conclusions

CeO_2 and MnO_x–CeO_2 nanomaterials were synthesized and used for the CWAO of phenol, whereby both CeO_2 and MnO_x–CeO_2 nanorods displayed superior catalytic activity than the cubic counterparts. The characterizations revealed that the catalytic activity can benefit from the presence of oxygen vacancies, which improves the reducibility of the catalyst surface and boosts the productivity of active oxygen species. The incorporation of Mn into the CeO_2 lattice can increase the phenol adsorption ability and further promote the oxidizing ability of the catalyst. Overall, this study illustrates the importance of oxygen vacancies in cerium catalysts for the CWAO of phenol, which might provide clues for a later study on other catalysts in this field.

Acknowledgements

The authors would like to thank the financial supports from the National Key Technology Support Program of China (No. 2014BAC10B01). Prof Dr Gai would like to thank the support from key scientific and technological project of China's Shanxi Province (No. MH2014-10). The support by the Natural Science Foundation of China (21336009 and 21673187) and the Natural Science Foundation of Fujian Province of China (No. 2015J05031) is also acknowledged.

References

1 S. Yang, W. Zhu, J. Wang and Z. Chen, *J. Hazard. Mater.*, 2008, **153**, 1248–1253.
2 I. P. Chen, S. S. Lin, C. H. Wang, L. Chang and J. S. Chang, *Appl. Catal., B*, 2004, **50**, 49–58.
3 C. B. Maugans and A. Akgerman, *Water Res.*, 1997, **31**, 3116–3124.
4 R. L. Autenrieth, J. S. Bonner, A. Akgerman, M. Okaygun and E. M. McCreary, *J. Hazard. Mater.*, 1991, **28**, 29–53.
5 W. Li, S. Zhao, B. Qi, Y. Du, X. Wang and M. Huo, *Appl. Catal., B*, 2009, **92**, 333–340.
6 A. B. Ayusheev, O. P. Taran, I. A. Seryak, O. Y. Podyacheva, C. Descorme, M. Besson, L. S. Kibis, A. I. Boronin, A. I. Romanenko and Z. R. Ismagilov, *Appl. Catal., B*, 2014, **146**, 177–185.
7 S. Yang, M. Besson and C. Descorme, *Appl. Catal., B*, 2015, **165**, 1–9.
8 S. S. Lin, C. L. Chen, D. J. Chang and C. C. Chen, *Water Res.*, 2002, **36**, 3009–3014.
9 S. Yang, Y. Cui, Y. Sun and H. Yang, *J. Hazard. Mater.*, 2014, **280**, 55–62.
10 S. Hamoudi, F. Larachi and A. Sayari, *J. Catal.*, 1998, **177**, 247–258.
11 S. Imamura, A. Doi and S. Ishida, *Ind. Eng. Chem. Prod. Res. Dev.*, 1985, **24**, 75–80.
12 S. Imamura, M. Nakamura, N. Kawabata, J. Yoshida and S. Ishida, *Ind. Eng. Chem. Prod. Res. Dev.*, 1986, **25**, 34–37.
13 F. Arena, G. Trunfio, J. Negro and L. Spadaro, *Appl. Catal., B*, 2008, **85**, 40–47.
14 S. X. Yang, X. G. Wang, H. W. Yang, Y. Sun and Y. X. Liu, *J. Hazard. Mater.*, 2012, **233**, 18–24.
15 F. Arena, C. Italiano, G. Drago Ferrante, G. Trunfio and L. Spadaro, *Appl. Catal., B*, 2014, **144**, 292–299.
16 F. Arena, J. Negro, A. Parmaliana, L. Spadaro and G. Trunfio, *Ind. Eng. Chem. Res.*, 2007, **46**, 6724–6731.
17 H. Zhang, X. Liu, N. Zhang, J. Zheng, Y. Zheng, Y. Li, C.-J. Zhong and B. H. Chen, *Appl. Catal., B*, 2016, **180**, 237–245.
18 A. C. Gluhoi, N. Bogdanchikova and B. E. Nieuwenhuys, *J. Catal.*, 2005, **229**, 154–162.
19 X. Liu, K. Zhou, L. Wang, B. Wang and Y. Li, *J. Am. Chem. Soc.*, 2009, **131**, 3140–3141.
20 Y. Y. Lin, Z. L. Wu, J. G. Wen, K. R. Poeppelmeier and L. D. Marks, *Nano Lett.*, 2014, **14**, 191–196.
21 S. Agarwal, L. Lefferts and B. L. Mojet, *ChemCatChem*, 2012, **5**, 479–489.
22 F. Lin, D. Hoang, C.-K. Tsung, W. Huang, S.-Y. Lo, J. Wood, H. Wang, J. Tang and P. Yang, *Nano Res.*, 2011, **4**, 61–71.
23 E. Aneggi, D. Wiater, C. de Leitenburg, J. Llorca and A. Trovarelli, *ACS Catal.*, 2014, **4**, 172–181.
24 X. Xing, Y. Cai, N. Chen, Y. Li, D. Deng and Y. Wang, *Ceram. Int.*, 2015, **41**, 4675–4682.
25 H. Li, G. Qi, Tana, X. Zhang, W. Li and W. Shen, *Catal. Sci. Technol.*, 2011, **1**, 1677.

26 P. Zhang, H. Lu, Y. Zhou, L. Zhang, Z. Wu, S. Yang, H. Shi, Q. Zhu, Y. Chen and S. Dai, *Nat. Commun.*, 2015, **6**, 8448–8458.
27 W. Cen, Y. Liu, Z. Wu, H. Wang and X. Weng, *Phys. Chem. Chem. Phys.*, 2012, **14**, 5769–5777.
28 S. P. Wang, L. F. Zhao, W. Wang, Y. J. Zhao, G. L. Zhang, X. B. Ma and J. L. Gong, *Nanoscale*, 2013, **5**, 5582–5588.
29 S. Liang, F. Teng, G. Bulgan, R. Zong and Y. Zhu, *J. Phys. Chem. C*, 2008, **112**, 5307–5315.
30 G. Hua, L. Zhang, G. Fei and M. Fang, *J. Mater. Chem.*, 2012, **22**, 6851–6855.
31 E. Bêche, P. Charvin, D. Perarnau, S. Abanades and G. Flamant, *Surf. Interface Anal.*, 2008, **40**, 264–267.
32 K. Niesz and D. E. Morse, *Nano Today*, 2010, **5**, 99–105.
33 S. Hamoudi, F. ç. Larachi, A. Adnot and A. Sayari, *J. Catal.*, 1999, **185**, 333–344.
34 D. Delimaris and T. Ioannides, *Appl. Catal., B*, 2008, **84**, 303–312.
35 P. Zhao, C. Wang, F. He and S. Liu, *RSC Adv.*, 2014, **4**, 45665–45672.
36 H. Chen, A. Sayari, A. Adnot and F. ç. Larachi, *Appl. Catal., B*, 2001, **32**, 195–204.
37 Z.-Y. Fei, B. Sun, L. Zhao, W.-J. Ji and C.-T. Au, *Chem.–Eur. J.*, 2013, **19**, 6480–6487.
38 G. Wang, B. B. Huang, Z. Z. Lou, Z. Y. Wang, X. Y. Qin, X. Y. Zhang and Y. Dai, *Appl. Catal., B*, 2016, **180**, 6–12.
39 W. Deng, Q. Dai, Y. Lao, B. Shi and X. Wang, *Appl. Catal., B*, 2016, **181**, 848–861.
40 H. Yao and Y. Y. Yao, *J. Catal.*, 1984, **86**, 254–265.
41 A. Trovarelli, *Catal. Rev.*, 1996, **38**, 439–520.
42 S. Zhang, X.-S. Li, B. Chen, X. Zhu, C. Shi and A.-M. Zhu, *ACS Catal.*, 2014, **4**, 3481–3489.
43 R. Zhang, K. Lu, L. Zong, S. Tong, X. Wang and G. Feng, *Appl. Surf. Sci.*, 2017, **416**, 183–190.
44 X. Tang, Y. Li, X. Huang, Y. Xu, H. Zhu, J. Wang and W. Shen, *Appl. Catal., B*, 2006, **62**, 265–273.
45 S. Nousir, S. Keav, J. Barbier Jr, M. Bensitel, R. Brahmi and D. Duprez, *Appl. Catal., B*, 2008, **84**, 723–731.